

Spectral Element Simulation of Liquid Metal Magnetohydrodynamics

Yichen Guo,^d Paul Fischer,^{a,b,c} and Misun Min^{*,a}

^a*Mathematics and Computer Science Division, Argonne National Laboratory
9700 S. Cass Avenue, Lemont, IL 60439*

^b*University of Illinois Urbana-Champaign, Department of Computer Science
201 N Goodwin Avenue, Urbana, IL 61801*

^c*University of Illinois Urbana-Champaign, Mechanical Science & Engineering
1206 W. Green Steet, Urbana, IL 61801*

^d*Virginia Tech, Department of Mathematics
225 Stranger Street, Blacksburg, VA 24060*

*Email: mmin@mcs.anl.gov

Number of pages: 25

Number of tables: 2

Number of figures: 12

Abstract

A spectral-element-based formulation of incompressible MHD is presented in the context of the open-source fluid-thermal code, Nek5000/RS. The formulation supports magnetic fields in a solid domain that surrounds the fluid domain. Several steady-state and time-transient model problems are presented as part of the code verification process. Nek5000/RS is designed for large-scale turbulence simulations, which will be the next step with this new MHD capability.

I. INTRODUCTION

Incompressible magnetohydrodynamics (MHD) describes the motion of electrically conducting fluids in a magnetic field. This coupled system for the velocity, \mathbf{u} , and magnetic field, \mathbf{B} , has been widely applied in various fields, including astrophysics and fusion. For fusion, there is significant interest in developing liquid metal breeder blankets, which involves transport under strong magnetic fields and high thermal loads. Here, we describe an extension of the spectral element thermal-fluid code, Nek5000/RS, to support incompressible MHD. Nek5000/RS is based on rapidly convergent matrix-free spectral element methods (SEM) that yield significant savings in computational resources for turbulent flow simulations. Nek5000 has scaled to $P > 10^6$ CPU cores [1] and NekRS has scaled to $P = 72,000$ GCDs on OLCF's AMD-based Frontier supercomputer [2].

Due to the strong coupling between a magnetic field and a velocity field resulting from the induction effect, the MHD system is more complicated than the Navier-Stokes equations that govern incompressible fluid motion alone. The MHD system involves two vector fields and, invariably, two Poisson equations, one for pressure and a magnetic pseudo-pressure, that act as Lagrange multipliers to keep each of the vector fields divergence-free. Additionally, the \mathbf{B} -field can take on nontrivial values in the solid vessel that surrounds the fluid domain, such that two domains are required to specify the governing equations.

II. GOVERNING EQUATIONS

We consider incompressible MHD defined on $\Omega_M = \Omega_F \cup \Omega_S$, where Ω_F is the fluid domain and Ω_S is the solid domain. The governing equations are

$$\frac{\partial \mathbf{u}}{\partial t} - \nu \nabla^2 \mathbf{u} + \nabla p = \mathbf{B} \cdot \nabla \mathbf{B} - \mathbf{u} \cdot \nabla \mathbf{u}, \quad (1)$$

$$\nabla \cdot \mathbf{u} = 0, \quad (2)$$

$$\frac{\partial \mathbf{B}}{\partial t} - \eta \nabla^2 \mathbf{B} + \nabla q = \mathbf{B} \cdot \nabla \mathbf{u} - \mathbf{u} \cdot \nabla \mathbf{B}, \quad (3)$$

$$\nabla \cdot \mathbf{B} = 0, \quad (4)$$

with \mathbf{u} , \mathbf{B} , p , and q the respective velocity, magnetic field, hydrodynamic pressure (divided by the density), and magnetic pressure. The kinematic viscosity and magnetic diffusivity are ν and η , respectively. We define initial conditions $\mathbf{u}(\mathbf{x}, t = 0) = \mathbf{u}^0$ and $\mathbf{B}(\mathbf{x}, t = 0) = \mathbf{B}^0$ and boundary conditions $\mathbf{u}(\mathbf{x}, t) = \mathbf{u}_b$ where Dirichlet conditions are applied on $\partial\Omega_{FD} \subset \partial\Omega_F$ and $\mathbf{B}(\mathbf{x}, t) = \mathbf{B}_b$ on $\partial\Omega_D \subset \partial\Omega_M$. Homogeneous Neumann conditions are defined on $\partial\Omega_{FN} \subset \partial\Omega_F$ and $\partial\Omega_{MN} \subset \partial\Omega_M$.

For the quadratic interaction terms on the right-hand side of (1) and (3) it is convenient to introduce Elsässer variables defined by $\mathbf{z}^\pm = \mathbf{u} \pm \mathbf{B}$, which give

$$\mathbf{u} = (\mathbf{z}^+ + \mathbf{z}^-)/2, \quad (5)$$

$$\mathbf{B} = (\mathbf{z}^+ - \mathbf{z}^-)/2. \quad (6)$$

Defining $\nu^\pm = (\nu \pm \eta)/2$, (equivalently $\nu = \nu^+ + \nu^-$ and $\eta = \nu^+ - \nu^-$), we can express the left-hand sides of Eqs. (1) and (3) as the following:

$$lhs^+ = \frac{\partial \mathbf{z}^+}{\partial t} - \nu^+ \nabla^2 \mathbf{z}^+ - \nu^- \nabla^2 \mathbf{z}^- + \nabla(p + q), \quad (7)$$

$$lhs^- = \frac{\partial \mathbf{z}^-}{\partial t} - \nu^+ \nabla^2 \mathbf{z}^- - \nu^- \nabla^2 \mathbf{z}^+ + \nabla(p - q). \quad (8)$$

Then the nonlinear terms on the right-hand sides of Eqs. (1) and (3) can be expressed by rhs^+

and rhs^- , respectively, as the following:

$$rhs^+ = -\mathbf{z}^- \cdot \nabla \mathbf{z}^+, \quad (9)$$

$$rhs^- = -\mathbf{z}^+ \cdot \nabla \mathbf{z}^-. \quad (10)$$

Thus we can write (7)–(10) in the following compact form:

$$\frac{\partial \mathbf{z}^\pm}{\partial t} - \nu^+ \nabla^2 \mathbf{z}^\pm - \nu^- \nabla^2 \mathbf{z}^\mp + \nabla(p \pm q) = -\mathbf{z}^\mp \cdot \nabla \mathbf{z}^\pm. \quad (11)$$

The attraction of (11) is its simplicity and symmetry, particularly regarding the rhs^\pm , which requires evaluation of only two convective substeps rather than the four that are required in the primitive-variable formulation (1)–(3). Unfortunately, if $\Omega_F \neq \Omega_M$, the full Elsässer formulation presents several challenge because \mathbf{u} and \mathbf{B} have boundary conditions in differing locations. Our approach therefore is to use (11) to generate the convection terms and to then convert these back to primitive variables using

$$rhs^{\mathbf{u}} = (rhs^+ + rhs^-)/2, \quad (12)$$

$$rhs^{\mathbf{B}} = (rhs^+ - rhs^-)/2. \quad (13)$$

In this way, the rhs^\pm terms require only two straightforward advection updates, (which can be done using either BDFk/EXTk or characteristics [3]). Note that z^\pm is defined everywhere by simply setting the fluid velocity $\mathbf{u} \equiv 0$ in Ω_S .

Finally, we have the following equations in nondimensional form for solving Eqs. (1)–(4):

$$\frac{\partial \mathbf{u}}{\partial t} - \frac{1}{Re} \nabla^2 \mathbf{u} + \nabla p = rhs^{\mathbf{u}}, \quad (14)$$

$$\frac{\partial \mathbf{B}}{\partial t} - \frac{1}{Rm} \nabla \cdot r_w \nabla \mathbf{B} + \nabla q = rhs^{\mathbf{B}}, \quad (15)$$

$$\nabla \cdot \mathbf{u} = 0, \quad (16)$$

$$\nabla \cdot \mathbf{B} = 0, \quad (17)$$

where $Re = UL/\nu$ and $Rm = UL/\eta$ are the Reynolds number and the magnetic Reynolds number,

respectively, and r_w reflects the change in η as one moves from the liquid to the supporting wall, Ω_S ,

$$r_w = 1 \text{ in } \Omega_F \tag{18}$$

$$r_w = \frac{\eta_S}{\eta} \text{ in } \Omega_S, \tag{19}$$

where η_S is the magnetic diffusivity in the solid, $\Omega_S := \Omega_M \setminus \Omega_F$.

III. NUMERICAL FORMULATION

In this section we describe our temporal and spatial discretizations including the weak formulation. Following the formulation used in Nek5000/RS [4], the temporal discretizations are based on k th-order backward difference formulas and extrapolation (BDF k /EXT k , $k = 1, 2$, or 3). Spatial discretizations are based on the spectral element method [5, 6].

III.A. Temporal Discretization

The terms on the left of (14)–(15) are treated implicitly, with the temporal derivative computed at time t^n using a k th-order backward difference formulation (BDF k),

$$\left. \frac{\partial \mathbf{u}}{\partial t} \right|_{t^n} \equiv \frac{1}{\Delta t} \sum_{j=0}^k \beta_j \mathbf{u}^{n-j} + O(\Delta t^k), \tag{20}$$

$$\left. \frac{\partial \mathbf{B}}{\partial t} \right|_{t^n} \equiv \frac{1}{\Delta t} \sum_{j=0}^k \beta_j \mathbf{B}^{n-j} + O(\Delta t^k), \tag{21}$$

where \mathbf{u}^{n-j} and \mathbf{B}^{n-j} denote the velocity and the magnetic field at time t^{n-j} , respectively. For the case of uniform timestep size Δt , $t^n = n\Delta t$, and the BDF k coefficients are $[\beta_0, \dots, \beta_k] = [-1, 1]$ for $k = 1$, $[3/2, -4/2, 1/2]$ for $k = 2$, and $[11/6, -18/6, 9/6, -2/6]$ for $k = 3$. The terms on the right of (14)–(15), which include nonlinear advection and any forcing terms are treated with k th-order

extrapolation. If $\mathbf{g} := r h s^{\mathbf{u}}$ and $\mathbf{h} := r h s^{\mathbf{B}}$, then the right-hand side of (14)–(15) are

$$\mathbf{g}|_{t^n} \equiv \sum_{j=1}^k \alpha_j \mathbf{g}^{n-j} + O(\Delta t^k), \quad (22)$$

$$\mathbf{h}|_{t^n} \equiv \sum_{j=1}^k \alpha_j \mathbf{h}^{n-j} + O(\Delta t^k). \quad (23)$$

For uniform Δt , we have $[\alpha_1, \dots, \alpha_k] = [1]$ for $k = 1$, $[2, -1]$ for $k = 2$, and $[3, -3, 1]$ for $k = 3$. For the semidiscretization in time, we drop the $O(\Delta t^k)$ residual terms and use (20)–(23) in (14)–(15). All other terms are evaluated implicitly at time t^n .

The first step in the splitting scheme is simply to sum all quantities known from previous timesteps, which amounts to constructing tentative velocity and magnetic fields,

$$\hat{\mathbf{u}} := \sum_{j=1}^k (-\beta_j \mathbf{u}^{n-j} + \Delta t \alpha_j \mathbf{g}^{n-j}), \quad (24)$$

$$\hat{\mathbf{B}} := \sum_{j=1}^k (-\beta_j \mathbf{B}^{n-j} + \Delta t \alpha_j \mathbf{h}^{n-j}). \quad (25)$$

As this step is just data collection, no boundary conditions are imposed in (24)–(25). The remaining implicit equations are linear, with the velocity and magnetic field solutions completely decoupled. Within each field, the individual *components* of each are still coupled because of the the divergence-free constraints, (16) and (17). Formally taking the divergence of (1) and (3) and requiring $\nabla \cdot \mathbf{u}^n = 0$ and $\nabla \cdot \mathbf{B}^n = 0$ lead to independent Poisson equations for the pressure and the magnetic pressure,

$$-\nabla^2 p^n = -\nabla \cdot \hat{\mathbf{u}} \text{ in } \Omega_F, \quad (26)$$

$$-\nabla^2 q^n = -\nabla \cdot \hat{\mathbf{B}} \text{ in } \Omega_M. \quad (27)$$

Boundary conditions for (26) and (27) are found by taking the dot product of (14)–(15) with the

outward-pointing unit normal on Ω_F and Ω_M , respectively, which yields

$$\nabla p^n \cdot \hat{\mathbf{n}} \Big|_{\partial\Omega_F} = \left(\frac{\hat{\mathbf{u}} - \beta_0 \mathbf{u}^n}{\Delta t} + \frac{1}{Re} \nabla^2 \mathbf{u}^n \right) \cdot \hat{\mathbf{n}} \Big|_{\partial\Omega_F}, \quad (28)$$

$$\nabla q^m \cdot \hat{\mathbf{n}} \Big|_{\partial\Omega_M} = \left(\frac{\hat{\mathbf{B}} - \beta_0 \mathbf{B}^n}{\Delta t} + \frac{1}{Rm} \nabla \cdot \frac{1}{r_w} \nabla \mathbf{B}^n \right) \cdot \hat{\mathbf{n}} \Big|_{\partial\Omega_M}. \quad (29)$$

We remark that \mathbf{u}^n is known on $\partial\Omega_F$ while $\nabla^2 \mathbf{u}^n$ is not. Similarly, \mathbf{B}^n is known on $\partial\Omega_M$ while $\nabla^2 \mathbf{B}^n$ is not. As with the nonlinear term, the unknown viscous and diffusivity terms can be treated explicitly after applying the vector identity

$$\nabla^2 \mathbf{u}^n = \nabla(\nabla \cdot \mathbf{u}^n) - \nabla \times (\nabla \times \mathbf{u}^n), \quad (30)$$

$$\nabla^2 \mathbf{B}^n = \nabla(\nabla \cdot \mathbf{B}^n) - \nabla \times (\nabla \times \mathbf{B}^n). \quad (31)$$

The first terms on the right of (30)–(31) are set to zero because of (16)–(17), so one only needs to extrapolate the curl of the vorticity, $\nabla \times (\nabla \times \mathbf{u}^n)$ on $\partial\Omega_{FD}$ and $\nabla \times (\nabla \times \mathbf{B}^n)$ on $\partial\Omega_{MD}$ [7]. Once the fluid pressure and magnetic pressure are known from (26)–(29), we can compute each component of $\mathbf{u}^n = [u_1^n \ u_2^n \ u_3^n]$ and $\mathbf{B}^n = [B_1^n \ B_2^n \ B_3^n]$ by solving a sequence of Helmholtz problems for \mathbf{u} and \mathbf{B} ,

$$-\frac{\Delta t}{Re} \nabla^2 u_i^n + \beta_0 u_i^n = \Delta t \left(\hat{u}_i - \frac{\partial p^m}{\partial x_i} \right), \quad i = 1, \dots, 3, \quad (32)$$

$$-\frac{\Delta t}{Rm} \nabla^2 B_i^n + \beta_0 B_i^n = \Delta t \left(\hat{B}_i - \frac{\partial q^m}{\partial x_i} \right), \quad i = 1, \dots, 3, \quad (33)$$

subject to appropriate boundary conditions on each component of \mathbf{u}^n and \mathbf{B}^n . In the case of mixed boundary conditions or variable diffusivities, we replace (32)–(33) by a pair of independent systems in which the individual components of velocity and magnetic field components are coupled. In either case, the viscous and diffusivity system will be diagonally dominant for modest to high Reynolds number applications given that $\Delta t/Re \ll 1$ and $\Delta t/Rm \ll 1$. For these cases, Jacobi preconditioned conjugate gradient iteration is an efficient solution strategy for the fully discretized form of (32)–(33).

III.B. Spatial Discretization

We use the spectral element method (SEM) [5], which is a high-order p -type finite element method (FEM) restricted to elements that are isoparametric images of the unit cube, $\hat{\Omega} := [-1, 1]^3$. On each element, Ω^e , $e = 1, \dots, E$, the solution and geometry are represented by tensor-product sums of N th-order Lagrange polynomials in $\hat{\Omega}$,

$$u(\mathbf{r}) \Big|_{\Omega^e} = \sum_{k=0}^N \sum_{j=0}^N \sum_{i=0}^N u_{ijk}^e h_i(r) h_j(s) h_k(t), \quad (34)$$

and

$$\mathbf{x}(\mathbf{r}) \Big|_{\Omega^e} = \sum_{k=0}^N \sum_{j=0}^N \sum_{i=0}^N \mathbf{x}_{ijk}^e h_i(r) h_j(s) h_k(t). \quad (35)$$

With nodal points ξ_j taken to be the Gauss-Lobatto-Legendre (GLL) quadrature points, this basis is *stable* and does not exhibit the Runge phenomenon often associated with high-order polynomials. Production values of N for NekRS are typically in the range 5–10, but we have run single element cases with Nek5000 up to $N = 100$. As noted in the early work of Orszag [8], restriction to tensor-product forms permits the use of fast *matrix-free* formulations in which operator evaluation is effected in $O(EN^4)$ operations and $O(EN^3)$ memory references for an E -element mesh, even in the case of deformed geometries. The number of grid points is $n \approx EN^3$, so the storage is only $O(n)$ and the work only $O(Nn)$, which is in sharp contrast to the standard FEM, where $O(nN^3)$ storage and work complexities typically compel a restriction to $N < 4$.

The elliptic subproblems (26)–(27) and (32)–(33) are cast in terms of variational projection operators. For example, for $u := u_i^n$ (the i th component of the velocity), the discrete form of (32) reads, *Find* $u \in X_0^N \subset \mathcal{H}_0^1$ *such that*

$$\frac{\Delta t}{Re} a(v, u) + \beta_0(v, u) = (v, f) \quad \forall v \in X_0^N. \quad (36)$$

Here, $(p, q) := \int_{\Omega} pq \, d\mathbf{x}$ is the standard L^2 inner product on Ω ; $a(p, q) := \int_{\Omega} \nabla p \cdot \nabla q \, d\mathbf{x}$ is the L^2 inner product of the gradients; X_0^N is the trial/test space comprising the spectral element basis functions; and \mathcal{H}_0^1 is the space of square-integrable functions on Ω that vanish on $\partial\Omega_D$ whose

gradient is also square-integrable. Formally expanding u in terms of trial functions $\phi_j(\mathbf{x})$ that span X_0^N , $u(\mathbf{x}) := \sum_{j=1}^n \phi_j(\mathbf{x})u_j$, and setting $v = \phi_i$, $i = 1, \dots, n$, leads to the matrix form of (36),

$$\frac{\Delta t}{Re} A \underline{u} + \beta_0 B \underline{u} = B \underline{f}, \quad (37)$$

where $\underline{u} = [u_1 \dots u_n]^T$ is the vector of unknown basis coefficients and \underline{f} is the vector of all known data, including the extrapolated nonlinear terms, boundary terms, and BDF k terms.

Here, we introduce respective stiffness, mass, and advection matrices having entries

$$A_{ij} = \int \nabla \phi_i \cdot \nabla \phi_j d\mathbf{x} \quad (38)$$

$$B_{ij} = \delta_{ij} \int \phi_i d\mathbf{x} \quad (39)$$

$$C(\mathbf{z})_{ij} = \int \phi_i \mathbf{z} \cdot \nabla \phi_j d\mathbf{x}, \quad (40)$$

where \mathbf{z} is a given advecting field (e.g., evaluation of (9) reads $-C(\mathbf{z}^-)\underline{\mathbf{z}}^+$). For the stiffness matrix, A , and mass matrix, B , it is standard practice in the SEM to replace integration by quadrature on the nodal points, which is effective because the rapid convergence of GLL quadrature for smooth functions. By contrast, it is important to use proper integration for the advection operator in order to ensure that C is skew-symmetric [9]. Over-integration with a 3/2s-rule increases operator complexity by about 4 \times , which is one of the reasons why the parsimonious Elsasser formulation of the nonlinear terms, given by (9)–(10) is attractive. The Elsasser formulation also makes clear that the physics of the nonlinear terms are effectively advection operators, with implied Courant-Friedrichs-Lewy (CFL) stability constraints that scale with characteristic velocity (U_0) and applied magnetic field strength (B_0). Stability regions for BDF k /EXT k can be found in [4].

III.C. Transient Hartmann Flow

In this subsection, we examine time-transient laminar Hartmann flow in a square duct. Since the flow is primarily in the x -direction and at low to moderate Reynolds numbers, as considered here, the solution remains invariant in x and varies only in the y and z directions. Under these

conditions, we can derive a simplified set of equations suitable for analysis and compare the analysis with the full MHD solution generated by NekRS. This allows us to assess both steady-state and asymptotic time-transient behavior as part of the code verification process.

In the test cases, we assume that we have conducting sidewalls of finite thickness δ . We define the fluid domain as $\Omega_F = [0, L] \times [-1, 1]^2$ with Dirichlet boundary conditions $\mathbf{u}|_{\partial\Omega_{FD}} = (0, 0, 0)$ and the magnetic field domain as $\Omega_M = [0, L] \times [-1 - \delta, 1 + \delta]^2$ with Dirichlet boundary condition $\mathbf{B}|_{\partial\Omega_{MD}} \equiv \mathbf{B}_0 = (0, B_0, 0)$. The initial conditions of velocity and magnetic field are zero. With an applied pressure gradient, $\frac{\partial p}{\partial x} = -\frac{1}{Re}$, the flow evolves to a steady state. We define $r_w = 1$ in the fluid domain, Ω_F , and r_w to be the ratio of the conductivity of the fluid domain to the electric conductivity of the sidewall, $\Omega_S := \Omega_M \setminus \Omega_F$. When $r_w \gg 1$, it is electrically insulating wall, which is equivalent to a Dirichlet condition for \mathbf{B} on Ω_M . When $r_w \ll 1$, it is a conducting wall, which corresponds to a Neumann condition for \mathbf{B} on Ω_M . The Hartmann number Ha is defined as $Ha := B_0 \sqrt{ReRm}$, which is a measure of the applied field strength.

Our solutions are marched to steady state from initial conditions $\mathbf{u} = (0, 0, 0)$ and $\mathbf{B} = \mathbf{B}_0$. With the chosen nondimensionalization, the steady state solution is independent of Re and Rm , so we take these to be unity in the fluid domain, unless otherwise indicated. The magnetic diffusivity in the solid domain is consequently r_w , which is set to $r_w = 10^2$, 1, and 10^{-5} . The first case corresponds to (nearly) electrically insulating walls while the last case corresponds to highly conducting walls. In the first case, the magnetic field is approximately equal to \mathbf{B}_0 everywhere in the wall and the same computational results can be attained by setting $\mathbf{B} := \mathbf{B}_0$ at the fluid boundary $\partial\Omega_F$.

Figure 1 shows the steady state axial velocity fields for the three boundary condition cases at $Ha = 10, 50$, and 100. Similar plots for $Ha = 10$ and 50 can be found in [10]. It can be seen that thin boundary layers, known as Hartmann layers, form at the Hartmann walls for large Ha , while somewhat thicker layers form at the sidewalls. Figure 3 shows the same data replotted as a surface mesh. For the insulating case in particular the flattening of the velocity profiles at high Ha is evident—the effect of the Lorentz force coupled with the induction equation is to suppress gradients of u in the channel center. Figures 2 and 4 show the corresponding distributions steady state axial magnetic fields for the cases of Figs. 1 and 3. Note that the magnetic field profile for

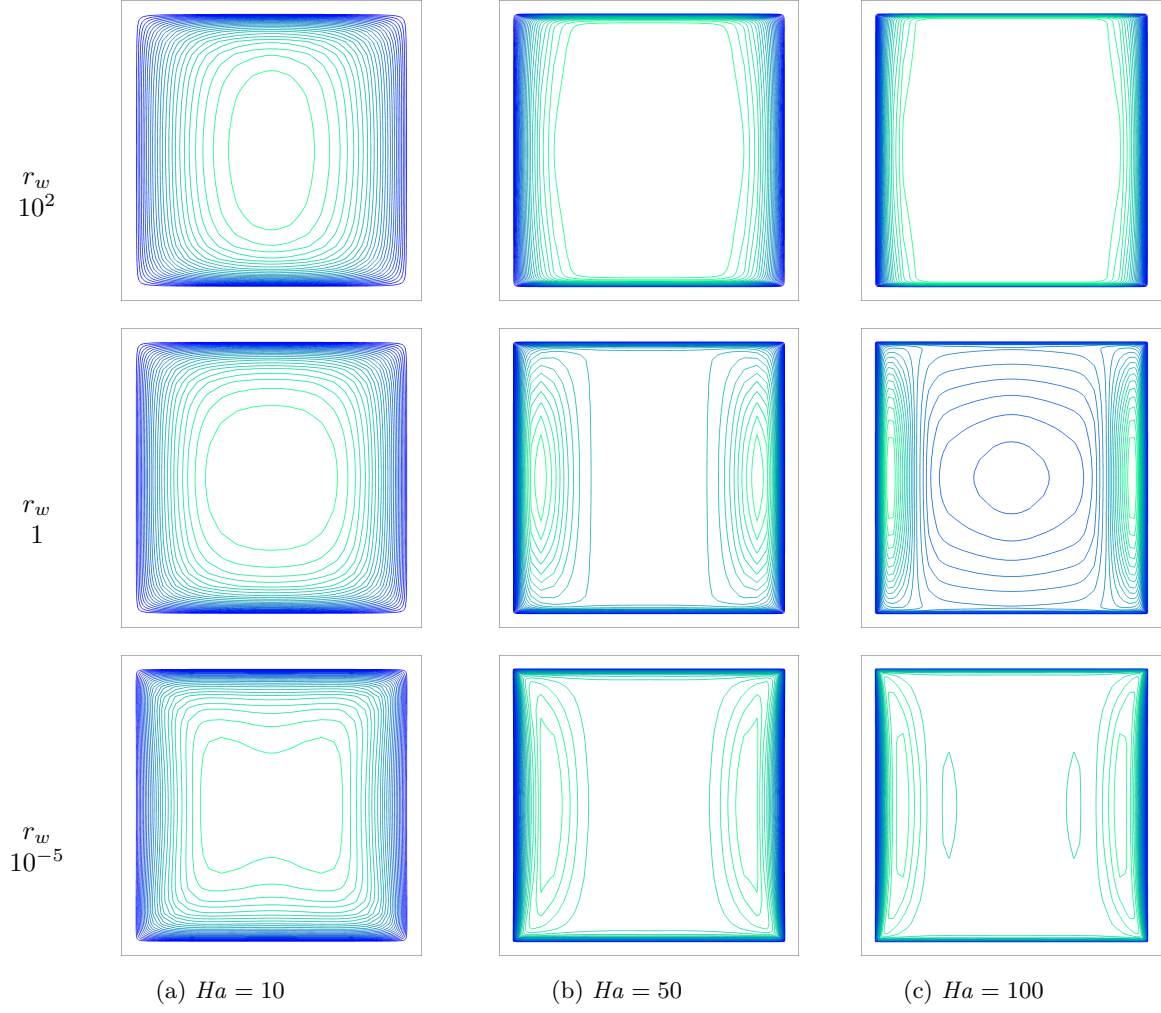


Fig. 1. Velocity distribution contour for $r_w = 10^2$, $r_w = 1$, and $r_w = 10^{-5}$ (bottom). $B_0 = Ha/\sqrt{ReRm} = 10, 50$, and 100 are used from left to right.

large Ha is essentially linear in y when the walls are highly conducting and does not form boundary layers in Ω_M . The case of perfectly conducting walls corresponds to Neumann conditions for \mathbf{B} on Ω_F and results in a singular condition for the steady-state solution because \mathbf{B} may be displaced by an arbitrary constant. This singularity motivated the consideration of walls having large, but finite, conductivity.

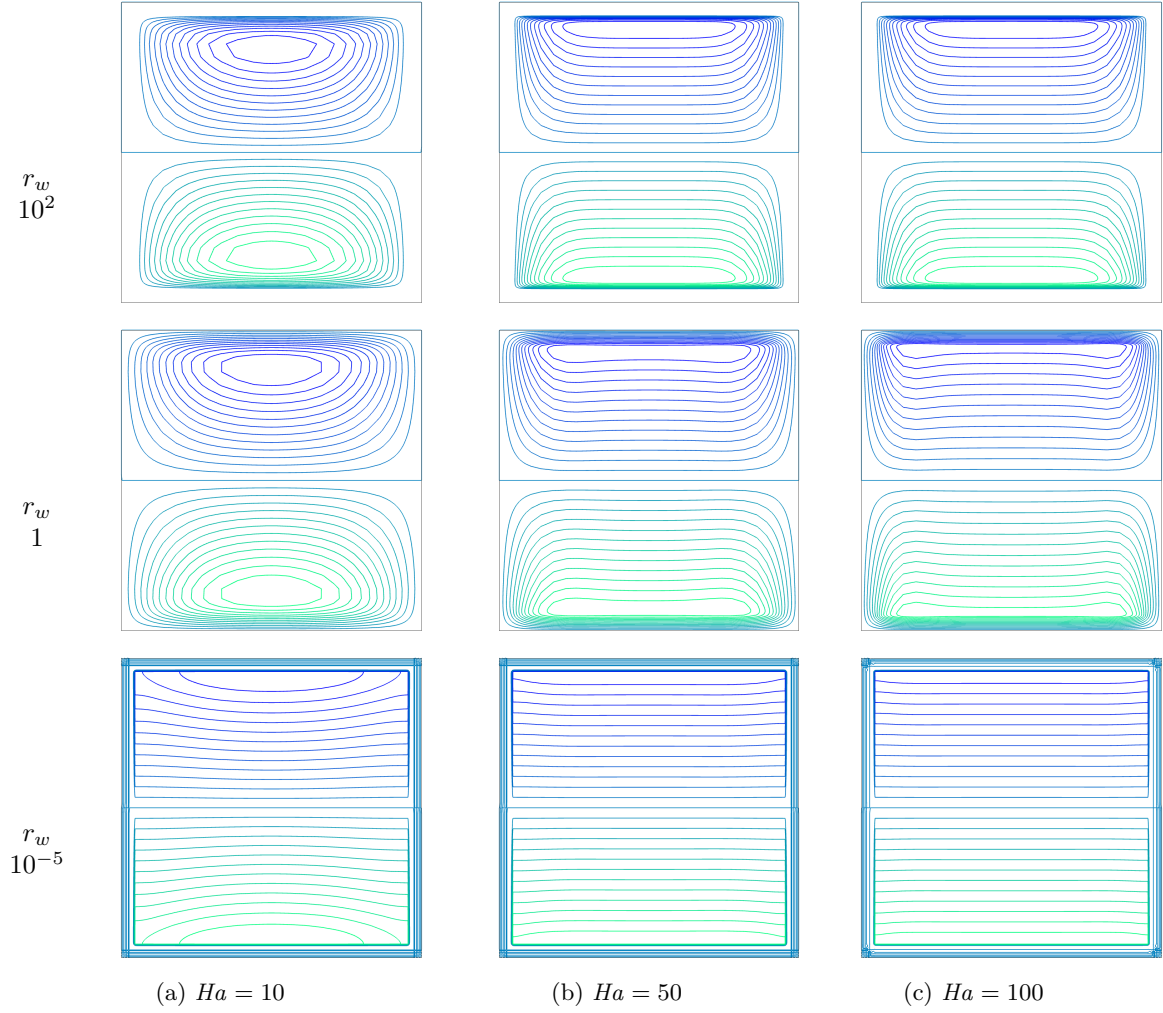


Fig. 2. Magnetic distribution contour for $r_w = 10^2$, $r_w = 1$, and $r_w = 10^{-5}$ (bottom). $B_0 = Ha/\sqrt{ReRm} = 10, 50$, and 100 are used from left to right.

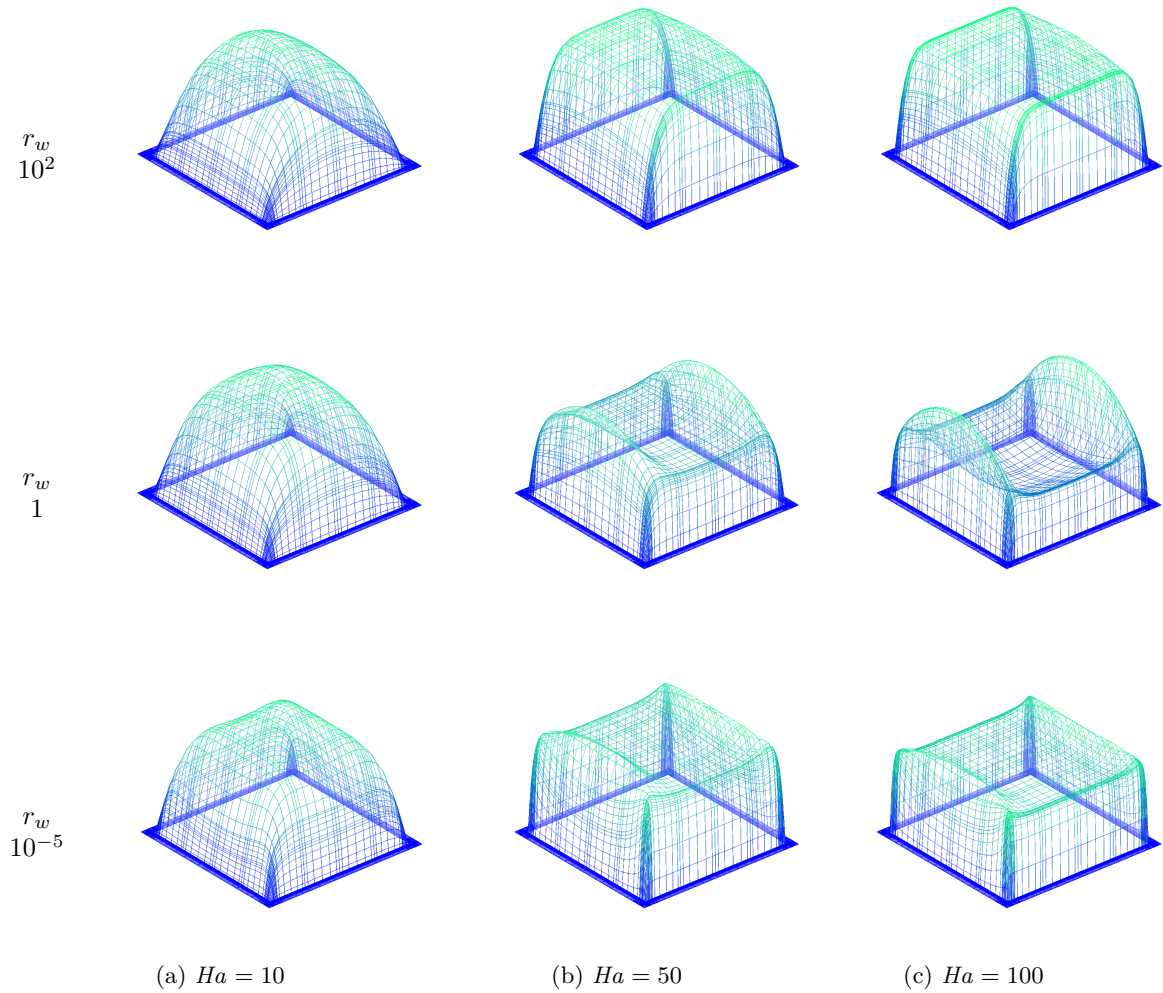


Fig. 3. Velocity distribution profile for $r_w = 10^2$, $r_w = 1$, and $r_w = 10^{-5}$ (bottom). $B_0 = Ha/\sqrt{ReRm} = 10, 50$, and 100 are used from left to right.

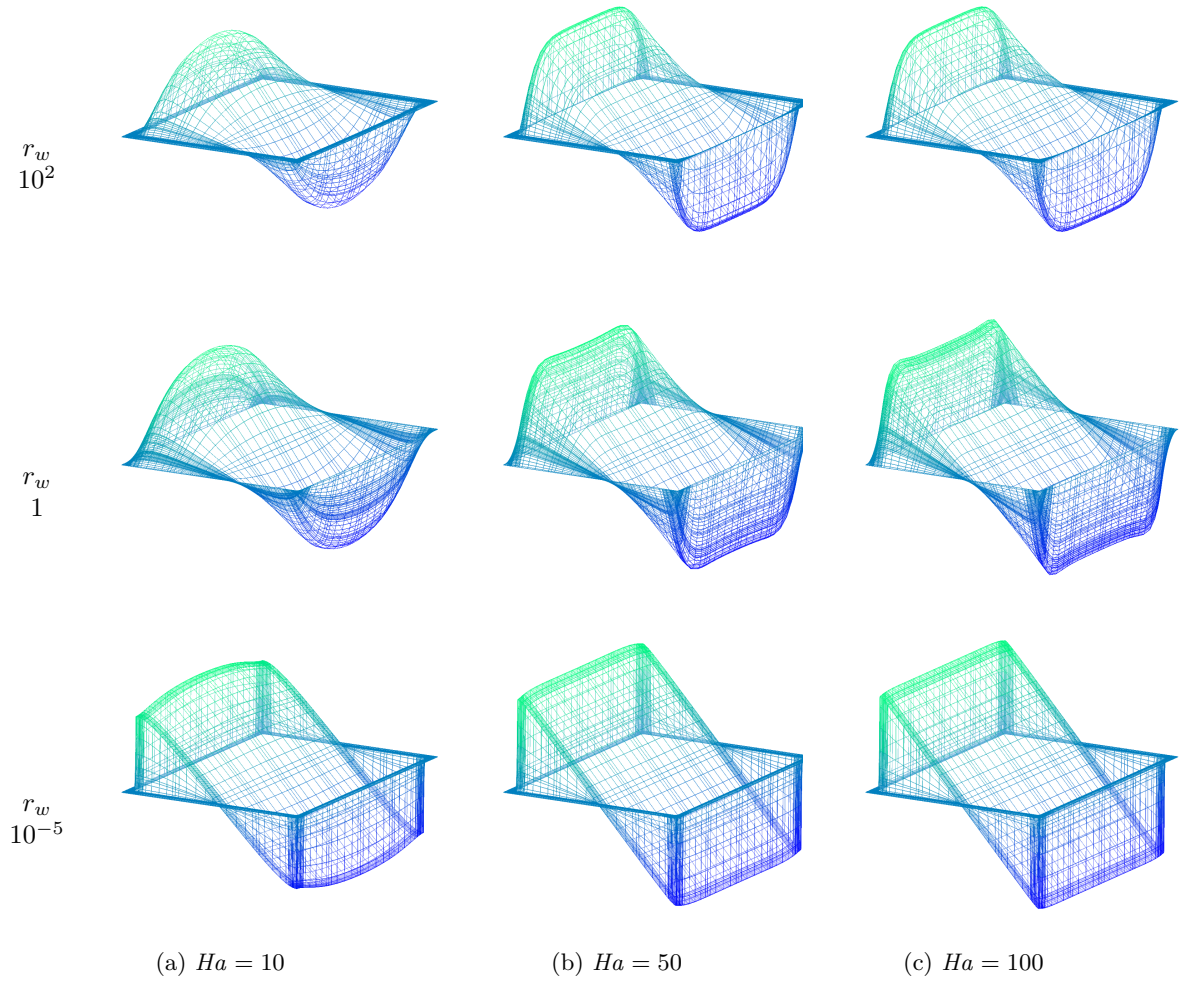


Fig. 4. Magnetic distribution profile for $r_w = 10^2$, $r_w = 1$, and $r_w = 10^{-5}$ (bottom). $B_0 = Ha/\sqrt{ReRm} = 10, 50$, and 100 are used from left to right.

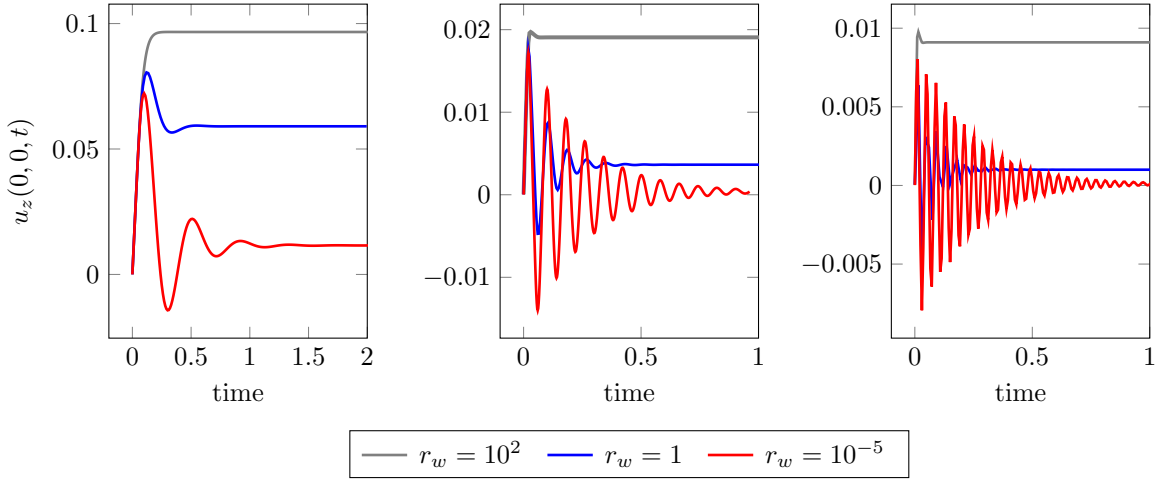


Fig. 5. Time histories of center-point velocity for $Ha = 10, 50, 100$ (left, middle, and right). $Re = Rm = 1$.

Analysis of Transient Response.

Because we are interested in simulation of turbulent flows, Nek5000/RS is intrinsically designed to solve the time-dependent MHD equations. All of the solutions of the preceding sections were thus computed in a time-stepping fashion and the transient responses in fact reveal interesting physics. Examples are shown in Fig. 5, where decaying and, potentially, oscillatory responses are evident, depending on Ha and r_w .

We analyze this behavior by deriving a simplified set of equations that model the transient response. We seek solutions of the form $\mathbf{u} = (u, 0, 0)$, $\mathbf{B} = (\tilde{b}, B_0, 0)$, where $u = u(y, z, t)$ is the x -component of the velocity and $\tilde{b} = \tilde{b}(y, z, t)$ is the x -component of the magnetic field. We note of course that this is not the only set of solutions—less trivial solutions will arise for sufficiently high (Re, Rm) . For sufficiently low Reynolds numbers, however, the flow is laminar and axially-independent, so that (1)–(4) reduce to

$$\frac{\partial u}{\partial t} - \frac{1}{Re} \nabla^2 u = B_0 \frac{\partial \tilde{b}}{\partial y} + \frac{1}{Re} \quad \text{in } \Omega_F, \quad (41)$$

$$\frac{\partial \tilde{b}}{\partial t} - \frac{r_w}{Rm} \nabla^2 \tilde{b} = B_0 \frac{\partial u}{\partial y} \quad \text{in } \Omega_M. \quad (42)$$

We apply homogeneous conditions for u on $\partial\Omega_F$. The boundary condition for magnetic field is

defined later. Note that $r_w \equiv 1$ in Ω_F .

To simplify the description of the steady-state solution, we presently take $r_w = 1$ and multiply (41) by Re and (42) by Rm to yield

$$\begin{aligned} Re \frac{\partial u}{\partial t} - \nabla^2 u - B_0 Re \frac{\partial \tilde{b}}{\partial y} &= 1, \\ Rm \frac{\partial \tilde{b}}{\partial t} - \nabla^2 \tilde{b} - B_0 Rm \frac{\partial u}{\partial y} &= 0. \end{aligned} \tag{43}$$

Recall that the Hartmann number is defined as $Ha := B_0 \sqrt{Re Rm}$. Let $\tilde{b} := \sqrt{\frac{Rm}{Re}} b$. Then

$$\begin{aligned} Re \frac{\partial u}{\partial t} - \nabla^2 u - Ha \frac{\partial b}{\partial y} &= 1, \\ Rm \frac{\partial b}{\partial t} - \nabla^2 b - Ha \frac{\partial u}{\partial y} &= 0. \end{aligned} \tag{44}$$

For the case of insulating walls, we have $u = 0$ on $\partial\Omega_F$ and $b = 0$ on $\partial\Omega_M$, and we can conveniently analyze (44). If $Re = Rm$, we rewrite the equation (44) in Elsasser variables $z^+ = u + b$ and $z^- = u - b$,

$$\begin{aligned} Re \frac{\partial z^+}{\partial t} - \nabla^2 z^+ - Ha \frac{\partial z^+}{\partial y} &= 1, \\ Re \frac{\partial z^-}{\partial t} - \nabla^2 z^- + Ha \frac{\partial z^-}{\partial y} &= 1. \end{aligned} \tag{45}$$

Coupled with homogeneous Dirichlet boundary conditions, (45) represents a pair of independent convection-diffusion equations. Consistent with the behavior in Fig. 5, these parabolic equations do not produce oscillatory solutions unless the initial condition is wavy. The boundary layer character of these equations as $t \rightarrow \infty$ is also well-understood in the high- Ha limit.

We remark that the conducting sidewall case $r_w = 10^{-5}$ is not simplified by the Elsasser formulation because the boundary conditions differ between u and b ; the velocity u satisfies homogeneous Dirichlet conditions while the magnetic field b satisfies homogeneous Neumann conditions.

Let (u_0, b_0) be the steady-state solution to (44) satisfying,

$$\begin{aligned} -\nabla^2 u_0 - Ha \frac{\partial b_0}{\partial y} &= 1, \\ -\nabla^2 b_0 - Ha \frac{\partial u_0}{\partial y} &= 0, \end{aligned} \tag{46}$$

which is governed by the single independent parameter, Ha , and the yet to be prescribed boundary conditions on b . For the fully conducting sidewall, Fig. 4 shows that the magnetic field is almost constant along x-direction. Thus, we assume that b_0 only depends on y . The weak form for (46) is

$$\begin{aligned} (\nabla u_0, \nabla \phi) - Ha \left(\frac{\partial b_0}{\partial y}, \phi \right) &= (1, \phi), \quad \forall \phi \in H_0^1(\Omega_F) \\ \left(\frac{\partial b_0}{\partial y}, \frac{\partial \psi}{\partial y} \right) &= Ha \left(\frac{\partial u_0}{\partial y}, \psi \right), \quad \forall \psi \in H^1(\Omega_M), \end{aligned} \tag{47}$$

Using integration-by-parts and the homogeneous Dirichlet conditions on u_0 , we obtain

$$\left(\frac{\partial b_0}{\partial y}, \frac{\partial \psi}{\partial y} \right) = -Ha \left(u_0, \frac{\partial \psi}{\partial y} \right).$$

The last equality implies

$$\left(\frac{\partial b_0}{\partial y}, \phi \right) = -Ha (u_0, \phi). \tag{48}$$

Inserting (48) into (47), we obtain a reaction diffusion equation for u_0 ,

$$(\nabla u_0, \nabla \phi) + Ha^2 (u_0, \phi) = (1, \phi) \tag{49}$$

Equation (49) is a singular perturbation problem with homogeneous Dirichlet boundary condition. When Ha is large, the center-point value, $u_0(0, 0)$, is close to $1/Ha^2$ [?, Part III, section 1].

To analyze the transient response, define $\bar{u} = u - u_0$ and $\bar{b} = b - b_0$. The functions \bar{u} and \bar{b} satisfy the homogeneous equivalent of (44),

$$\begin{aligned} Re \frac{\partial \bar{u}}{\partial t} - \nabla^2 \bar{u} - Ha \frac{\partial \bar{b}}{\partial y} &= 0, \\ Rm \frac{\partial \bar{b}}{\partial t} - \nabla^2 \bar{b} - Ha \frac{\partial \bar{u}}{\partial y} &= 0, \end{aligned} \tag{50}$$

We proceed with the ansatz that u has a modal expansion of the form

$$u(y, z, t) = \sum_{k=0}^{\infty} \sum_{l=0}^{\infty} \sum_{k=0}^{\infty} \sum_{l=0}^{\infty} \hat{u}_{kl}(t) \cos\left(\frac{\pi}{2}(2k+1)y\right) \cos\left(\frac{\pi}{2}(2l+1)z\right), \quad (51)$$

which satisfies the homogeneous Dirichlet boundary conditions and matches the even symmetry of the data and initial conditions. Given that (44) contains a first derivative of u with respect to y , we must assume that b has the form

$$b(y, z, t) = \sum_{k=0}^{\infty} \sum_{l=0}^{\infty} \hat{b}_{kl}(t) \sin\left(\frac{\pi}{2}(2k+1)y\right) \cos\left(\frac{\pi}{2}(2l+1)z\right), \quad (52)$$

which is consistent with (44) and (51). We are interested in the time-transient response of the most slowly decaying mode. Inserting (51) and (52) into (44) and retaining only the lowest ($k = l = 0$) modes leads to

$$\begin{aligned} Re\hat{u}_t + \frac{\pi^2}{2}\hat{u} - Ha\frac{\pi}{2}\hat{b} &= 0 \\ Rm\hat{b}_t + \frac{\pi^2}{2}\hat{b} + Ha\frac{\pi}{2}\hat{u} &= 0 \end{aligned} \quad (53)$$

where $\hat{u} := \hat{u}_{00}$ and $\hat{b} := \hat{b}_{00}$.

Let $q := (\hat{u}, \hat{b})^T$. Then (53) has the form $\underline{q}_t + Aq = 0$, with

$$A := \begin{bmatrix} \frac{\pi^2}{2Re} & -\frac{\pi}{2}\frac{Ha}{Re} \\ \frac{\pi}{2}\frac{Ha}{Rm} & \frac{\pi^2}{2Rm} \end{bmatrix}. \quad (54)$$

The eigenvalues of A are of the form $s \pm iw$, where s and w are real with values

$$\begin{aligned} s &= \frac{\pi^2}{4} \left(\frac{1}{Re} + \frac{1}{Rm} \right), \\ w &= \frac{\pi}{2} \frac{Ha}{\sqrt{ReRm}} \left(1 - \frac{\pi^2}{4Ha^2} \frac{(Rm - Re)^2}{RmRe} \right)^{\frac{1}{2}}. \end{aligned} \quad (55)$$

Combining the first-mode transient with the steady state solution to (44) leads to the asymptotic transient response,

$$u \sim \hat{u}_0 e^{-st} \sin(\omega t + \phi) + \frac{1}{Ha^2}, \quad (56)$$

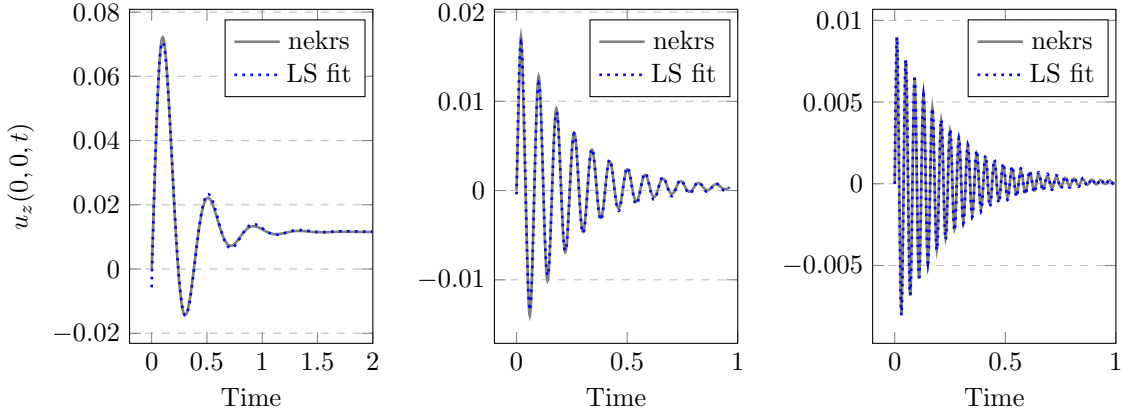


Fig. 6. Model fit of the center-point velocity to the NekRS results for $Ha = 10, 50, 100$ (left, middle, and right) with conducting walls ($r_w = 10^{-5}$) for $Re = Rm = 1$. A nonlinear fit is used to approximate $\hat{u}_0, s, \omega, \phi$ and s_0 in $\hat{u} = \hat{u}_0 e^{-st} \sin(\omega t + \phi) + s_0$.

To leading order in Ha (exact for the case $Re = Rm$), (55) implies a period $\tau = 4/Ha$ with a decaying envelope of the form e^{st} , which is in excellent agreement with the behavior observed in the simulations.

Figure 6 shows the decay rate of the centerline velocity for the case $Ha = 10, 50, 100$ with $Re = Rm = 1$ compared with the model

$$u \sim \hat{u}_0 e^{-st} \sin(\omega t + \phi) + s_0, \quad (57)$$

where $\hat{u}_0, s, \omega, \phi$ and s_0 are determined by a nonlinear fit using Levenberg-Marquardt.

Table I shows the approximate values of the decay rate and frequency via the nonlinear fit and the analytic values from (55) for various $Ha = 10, 50, 100$. The results indicate that the approximate decay rate is slightly higher than the analytic value, likely due to the analysis considering only the dominant term, while higher-order terms exhibit faster decay rates. In contrast, the approximate frequency and steady-state value show good agreement with the analytic values. Figure 7 illustrates the time history of the center-point velocity, using the analytic decay rate and frequency from equation (55), while employing a nonlinear fit to determine only \hat{u}_0 and ϕ . The asymptotic results are in good agreement with the numerical results.

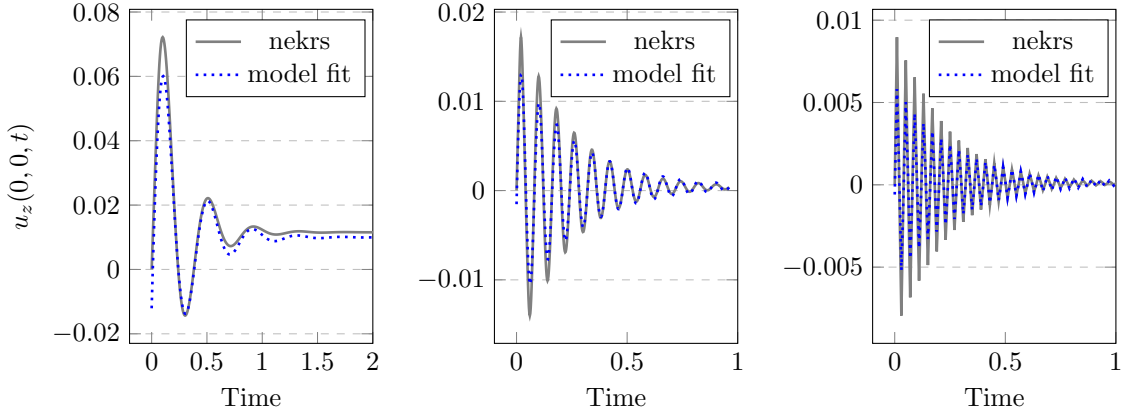


Fig. 7. Time history of center-point velocity for $Ha = 10, 50, 100$ with conducting walls ($r_w = 10^{-5}$) for $Re = Rm = 1$. A nonlinear fit is used to approximate \hat{u}_0 and ϕ in the model $\hat{u} = \hat{u}_0 e^{-st} \sin(\omega t + \phi) + \frac{1}{Ha^2}$. Parameters s and ω are calculated from (54).

Hartmann number	$Ha = 10$		$Ha = 50$		$Ha = 100$	
	approx.	analytic	approx.	analytic	approx.	analytic
decay rate s	3.95	3.70	4.19	3.70	4.11	3.70
frequency ω	15.27	15.61	156.87	157.07	78.35	78.52
steady state s_0	0.012	0.01	0.97×10^{-4}	1×10^{-4}	3.5×10^{-4}	4×10^{-4}

TABLE I

Comparison of decay rate, frequency, and steady state of center-point velocity fitted by Levenberg-Marquardt method.

IV. TEST CASES

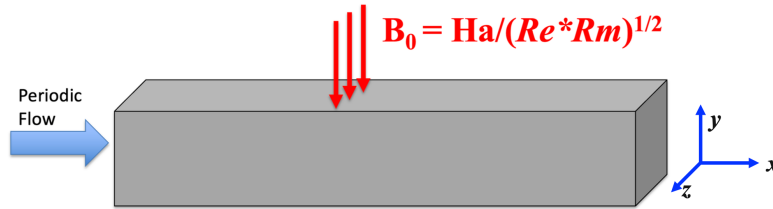


Fig. 8. Laminar flow in a square duct with an applied magnetic field.

In this section, we explore several Hartmann flow cases using the axially-periodic duct configuration of Fig. 8. Here, the flow is forced in the x direction and an external magnetic field of strength B_0 is applied in the $-y$ direction. The first two cases, Shercliff flow and Hunt flow, have closed-form steady-state solutions that can be used to establish spatial convergence. Subsequently, we explore novel asymptotic approximations to the time-transient response of impulsively-started Hartmann flow and compare these with the observed response of NekRS in order to check correctness of the

	r_w	$\gg 1$	$\ll 1$
B	Solid Domain	Insulating	Conducting
	Boundary Behaviors	Dirichlet	Neumann
u	Decay Rate	–	$\frac{\pi^2}{4} \left(\frac{1}{Re} + \frac{1}{Rm} \right)$
	Frequency	–	$\frac{\pi}{2} \frac{Ha}{\sqrt{ReRm}} \left(1 - \frac{\pi^2}{4Ha^2} \frac{(Rm-Re)^2}{RmRe} \right)^{\frac{1}{2}}$
	Steady Solution $u(0,0)$	$\frac{1}{Ha}$	$\frac{1}{Ha^2}$

TABLE II

Description of the behaviors of **B** on the solid domain Ω_S and on the boundary $\partial\Omega_{MD}$, and the decay rate, frequency and steady state solution of **u** for the Hartmann flows, depending on the electric conductivity ratio r_w . Dirichlet boundary conditions are used for both **B** and **u** for the Hartmann flow simulations.

MHD temporal discretization.

As an initial verification case, we consider laminar flow in a square duct with a fixed mean pressure gradient $\frac{\partial p}{\partial x} = -\frac{1}{Re}$ and an applied magnetic field, $\mathbf{B}_0 := (0, B_0, 0)$, as illustrated in Fig. ???. We impulsively start the flow in the x -direction. The simulations are carried out with periodic boundary conditions in x . We define the fluid domain as $\Omega_F = [0, L] \times [-1, 1]^2$ with Dirichlet boundary conditions $\mathbf{u}|_{\partial\Omega_{FD}} = (0, 0, 0)$. The solid domain and magnetic boundary conditions are defined later based on the problem. The initial conditions of velocity and magnetic field are zero. With the applied pressure gradient, the flow evolves to a steady state for the relatively low Reynolds numbers considered in these examples.

IV.A. Shercliff flow

In this subsection, we examine a square channel flow with insulating walls using the analytic solutions provided in [10] for $Ha = 10, 50, 100$. For the first case, we consider $\Omega_M \equiv \Omega_F$, applying homogeneous Dirichlet boundary conditions for both the velocity and magnetic fields on $\partial\Omega_F$. Figure 9 shows the numerical and analytic solutions for velocity and magnetic fields at $Ha = 10, 50, 100$, using a polynomial order of $N = 6$. The strong agreement between the two demonstrates correctness of the spatial operators. We establish the convergence rate by varying the polynomial degree from $N = 2$ to 8. Exponential convergence is clear in the semi-log plot of Fig. 10, which shows the relative L^∞ error for the velocity and magnetic fields versus N .

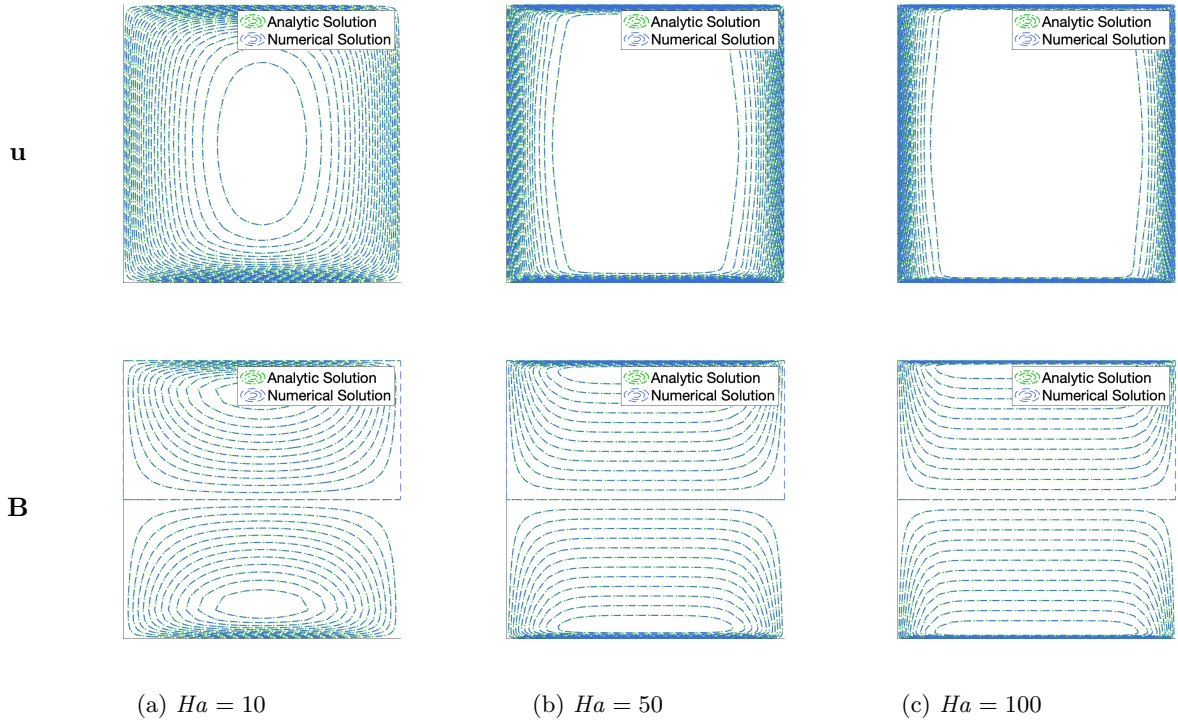


Fig. 9. Velocity (top) and magnetic (bottom) distribution contour of the numerical solution and the analytic solution for $Ha = 10, 50, 100$ and polynomial order $N = 6$.

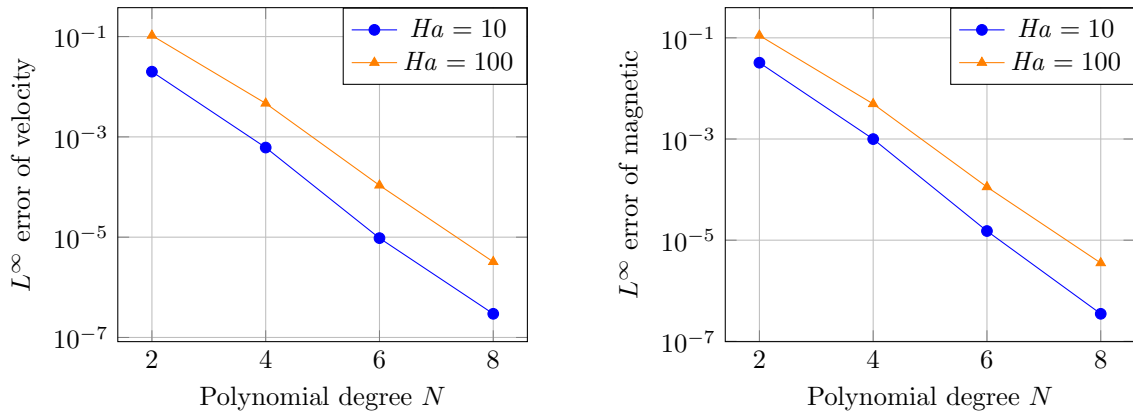


Fig. 10. Convergence for Shercliff flow: the relative L^∞ error of velocity (left) and magnetic (right) fields with the polynomial degree N varying from 2 to 8 and using $4 \times 10 \times 10$ elements. The problem considered is flow in rectangular channels on the domain $[0, 4] \times [-1, 1] \times [-1, 1]$ with insulating walls and $Re = Rm = 1$. An analytic solution [10, ?, eq. (4.37)] is used to compute the error.

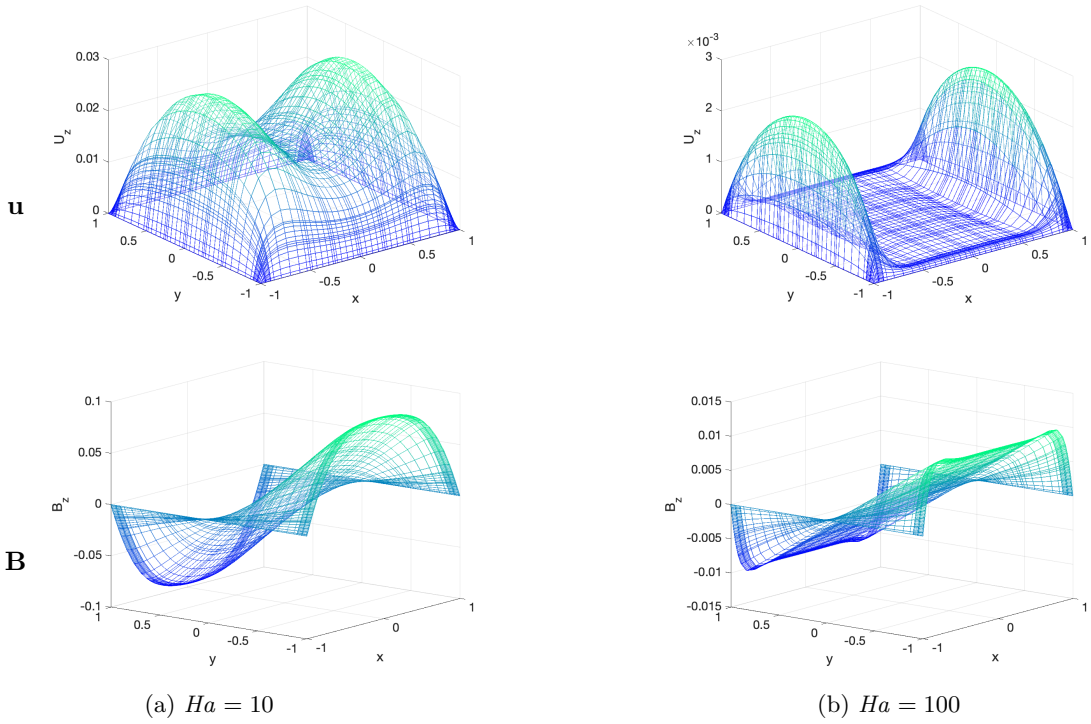


Fig. 11. Velocity(above) and magnetic(below) distribution of the numerical solution for Hunt flow with $Ha = 10$ and $Ha = 100$, perfectly conducting and insulating walls, and polynomial order $N = 6$.

IV.B. Hunt flow

In [11], an analytic solution is provided for the Hunt flow problem. The duct has perfectly conducting walls perpendicular to the applied magnetic field and insulating walls parallel to it. Velocity has homogeneous Dirichlet boundary conditions on the walls, while the magnetic field has homogeneous Neumann boundary conditions on the conducting walls and homogeneous Dirichlet boundary conditions on the insulating walls. Figure 11 shows the numerical solution of velocity and magnetic fields for $Ha = 10$ and $Ha = 100$ with $N = 6$ and $4 \times 10 \times 10$ elements. Comparing with the analytic solution, the convergence of the relative L^∞ error of velocity and magnetic fields is shown in Fig. 12 with varying polynomial degrees from 2 to 8.

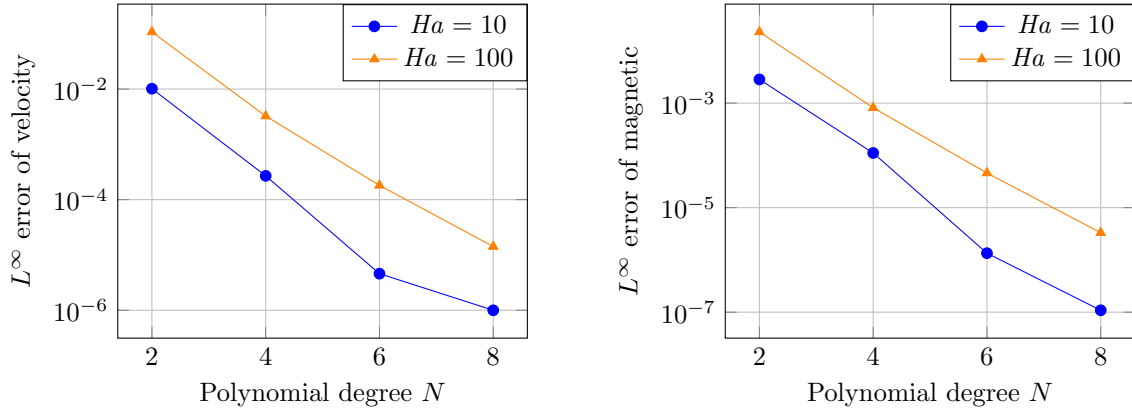


Fig. 12. Convergence of the relative L^∞ error of velocity (left) and magnetic (right) fields with the polynomial degree N varying from 2 to 8 and using $4 \times 10 \times 10$ elements. The problem considered is Hunt flow in rectangular channels on the domain $[0, 4] \times [-1, 1] \times [-1, 1]$ with perfectly conducting and insulating walls and $Re = Rm = 1$. An analytic solution [11, ?] is used to compute the error.

V. CONCLUSION

This article introduces a new MHD capability into the highly-scalable thermal-fluid simulation code, Nek5000/RS, and demonstrates basic verification results including exponential convergence to known analytical steady-state solutions and consistent results with novel time-transient responses based on asymptotic analysis. The code has been recently applied to turbulent MHD Hartmann flows and validation of these results is ongoing.

ACKNOWLEDGMENTS

This material is based upon work supported by the U.S. Department of Energy, Office of Science, under contract DE-AC02-06CH11357 and by the Exascale Computing Project (17-SC-20-SC), a collaborative effort of two U.S. Department of Energy organizations (Office of Science and the National Nuclear Security Administration).

REFERENCES

- [1] P. FISCHER, K. HEISEY, and M. MIN, “Scaling Limits for PDE-Based Simulation (Invited),” *22nd AIAA Computational Fluid Dynamics Conference, AIAA Aviation*, AIAA 2015-3049 (2015).

- [2] E. MERZARI, S. HAMILTON, T. EVANS, P. ROMANO, P. FISCHER, M. MIN, S. KERKEMEIER, Y. LAN, J. FANG, M. PHILLIPS, T. RATHNAYAKE, E. BIONDO, K. ROYSTON, N. CHALMERS, and T. WARBURTON, “Exascale Multiphysics Nuclear Reactor Simulations for Advanced Designs (Gordon Bell Prize Finalist paper),” *Proc. of SC23: Int. Conf. for High Performance Computing, Networking, Storage and Analysis*, IEEE (2023).
- [3] S. PATEL, P. FISCHER, M. MIN, and A. TOMBOULIDES, “A Characteristic-Based, Spectral Element Method for Moving-Domain Problems,” *J. Sci. Comp.*, **79**, 564 (2019).
- [4] P. FISCHER, M. SCHMITT, and A. TOMBOULIDES, *Recent developments in spectral element simulations of moving-domain problems*, vol. 79, 213–244, Fields Institute Communications, Springer.
- [5] A. PATERA, “A spectral element method for fluid dynamics : laminar flow in a channel expansion,” *J. Comput. Phys.*, **54**, 468 (1984).
- [6] M. DEVILLE, P. FISCHER, and E. MUND, *High-order methods for incompressible fluid flow*, Cambridge University Press, Cambridge (2002).
- [7] A. TOMBOULIDES, M. ISRAELI, and G. KARNIADAKIS, “Efficient Removal of Boundary-Divergence Errors in Time-Splitting Methods,” *J. Sci. Comput.*, **4**, 291 (1989).
- [8] S. ORSZAG, “Spectral methods for problems in complex geometry,” *J. Comput. Phys.*, **37**, 70 (1980).
- [9] J. MALM, P. SCHLATTER, P. FISCHER, and D. HENNINGSON, “Stabilization of the Spectral-Element Method in convection dominated flows by recovery of skew symmetry,” *J. Sci. Comp.*, **57**, 254 (2013).
- [10] U. MÜLLER and L. BÜHLER, *Magnetofluidynamics in channels and containers*, Springer Science & Business Media (2001).
- [11] J. HUNT, “Magnetohydrodynamic flow in rectangular ducts,” *Journal of fluid mechanics*, **21**, 4, 577 (1965).